Nano Research 2017, 10(8): 2782–2799
DOI 10.1007/s12274-017-1482-x
Research Article
ISSN 1998-0124
CN 11-5974/O4

Engineering a tubular mesoporous silica nanocontainer with well-preserved clay shell from natural halloysite

Liangjie Fu[1,2], Huaming Yang[1,3] (✉), Aidong Tang[4], and Yuehua Hu[1,3] (✉)

[1] *Centre for Mineral Materials, School of Minerals Processing and Bioengineering, Central South University, Changsha 410083, China*
[2] *Peter A. Rock Thermochemistry Laboratory and NEAT ORU, University of California Davis, One Shields Avenue, Davis, CA 95616, USA*
[3] *Hunan Key Lab of Mineral Materials & Application, Central South University, Changsha 410083, China*
[4] *School of Chemistry and Chemical Engineering, Central South University, Changsha 410083, China*

Received: 13 November 2016
Revised: 23 December 2016
Accepted: 14 January 2017

KEYWORDS
halloysite,
mesoporous nanotubes,
acid leaching,
hydrothermal synthesis,
density functional theory (DFT) calculation,
nanocontainer

ABSTRACT

The *in situ* synthesis of mesoporous nanotubes from natural minerals remains a great challenge. Herein, we report the successful synthesis of mesoporous silica nanotubes (MNTs) with a varying inner-shell thickness and a preserved clay outer shell from natural-halloysite nanotubes (HNTs). After the enlargement of the lumen diameter of the tubular aluminosilicate clay by acid leaching, uniform mesopores were introduced by a modified pseudomorphic transformation approach, while the clay outer shell was well-preserved. Using density functional theory calculations, the atomic structure evolution and the energetics during Al leaching and Si–OH condensation were studied in detail. After the leaching of Al ions from the HNTs, local structural changes from Al(Oh) to Al(V) at a medium leaching level and to Al(Td) at a high leaching level were confirmed. The calculated hydroxylation energy of two kinds of silica components in the acid-leached HNTs (the distorted two-dimensional silica source in the inner shell and the intact aluminosilicate structure in the outer shell) was 0.5 eV lower or 1.0 eV higher than that of bulk silica, which clarifies the different behavior of the silica components in the hydrothermal process. The successful synthesis of reactive MNTs from HNTs introduces a new strategy for the synthesis of mesoporous nanocontainers with a special morphology using natural minerals. In particular, MNT samples with numerous reactive Al(V) species and a specific surface area up to 583 m^2/g (increased by a factor of 10) are promising drug-loading nanocontainers and nanoreactors.

1 Introduction

Recently, with the maturity of synthesis technology for mesoporous silica materials, the morphology control of silica has been well-developed, including spheres [1, 2], beans [3], fibers [4], and tubes [5]. While

Address correspondence to Huaming Yang, hmyang@csu.edu.cn; Yuehua Hu, hyh@csu.edu.cn

the nanoconfinement of the mesoporous structure prevents the sintering of supported catalysts [6], the tubular structure has shown unique chemical and physical properties for adsorption, separation, and drug delivery [7–11]. Natural-halloysite nanotubes (HNTs), compared with synthetic silica tubes and other nanotubes such as C [12, 13], boron nitride [14], and metal-oxide nanotubes [15], are an economically viable alternative. Because they can be mined as a raw mineral, they are also eco-friendly and biocompatible [16, 17]. Owing to the potential applications of halloysite in adsorption [18, 19], controlled release [20–22], nanocontainers [23], nanoreactors [24], and polymer composites [25], the selective modification of halloysite lumen has attracted increasing attention recently [20, 21, 26–28].

The performance of nanotubular materials depends on the tunability of the diameters. The inner diameters and wall thickness of mesoporous silica nanotubes (MNTs) can be tailored by changing the gel composition [29] or the diameter of the template [30]. As a traditional chemical activation method, acid-leaching treatment was demonstrated as an effective method for improving the tube lumen capacity (by decreasing the wall thickness), surface area (by up to 250 m^2/g), and loading efficiency of natural halloysite. After the kinetic analysis of acid leaching under different temperatures and acid concentrations, the variation of the stability and pore characteristics of HNTs in acid/base solutions was reported [20, 31–33]. Acid or base treatment were performed to produce lumen-enlarged HNTs [20, 34], silica nanotubes [35], and mesoporous materials when the pseudomorphic transformation method was used [36, 37]. Here, clay nanoparticles were used as the framework source instead of silica nanoparticles [38, 39].

However, because of the difficulty of distinguishing structural changes in clay minerals when the intermediate phases are poorly crystalline [40], the details regarding the atomic structure evolution and energetics during acid leaching and the hydrothermal process remain unclear. All natural nanoparticles have hydrated surfaces, where the surface concentrations of H^+, H_2O, and OH^- depend on the pH. The surface hydration, hydroxylation, protonation, and surface precipitates involving these adsorbates are complicated [41]. Many hydrated aluminosilicates can have a thermodynamic stability field near room temperature. The enthalpy of hydration becomes less exothermic as the water content increases, which makes the surface properties more complicated [42].

Herein, a novel approach for synthesizing MNTs from HNTs by introducing mesopores inside the lumen structure of natural-halloysite nanotubes is proposed. Using modified pseudomorphic transformation methods, well-defined MNTs with a tunable mesoporous silica inner shell and a preserved clay outer shell, which are promising drug-loading nanocontainers, are obtained by exploiting the chemical components and the morphology of natural clay. The acid leaching and silica condensation are investigated by experimental characterizations and density functional theory (DFT) calculations. The atomic structure evolution (especially the local structural change of Al–OH and Si–O) and the energetics involved are clarified in detail. Introducing mesoporous structures in the inner walls of the acid-leached halloysite clay shell (typically 50% dealumination) yields an excellent eco-friendly nanocontainer for Ag loading.

2 Experimental

2.1 Acid leaching of HNTs

HNTs were pretreated via emulsion dispersion, filtering, washing with distilled water, and drying for 8 h at 80 ℃. Then, 3 g of the pretreated HNTs were treated with 750 mL of a hydrochloric acid (HCl) solution at different acid concentrations (1–6 M) and temperatures (50–100 ℃) under constant stirring for different amounts of time (ranging from 0.5 h to 10 days). The suspension was then filtered, washed with distilled water, and dried at 80 ℃ overnight. We denote the acid-leached samples pretreated at an acid concentration of 6 M and a solution temperature of 100 ℃ for x h as leached HNTs-xh.

2.2 Synthesis of MNTs

In a typical experiment, 1 g of the leached sample was added to a cetyltrimethylammonium bromide (CTAB) solution (1 g of CTAB and 50 mL of distilled water), and the pH of mixture was adjusted to

10.5 using a 0.5 M NaOH solution. The mixture was stirred for 3 h at 60 ℃, transferred to a Teflon-lined steel autoclave, and then statically heated at 100 ℃ for 24 h. The white powder resultant was filtered, washed, and dried at 80 ℃ overnight. The resulting as-synthesized material was calcined at 550 ℃ for 6 h in air at a heating rate of 2 ℃/min to form MNTs. MNTs obtained with an acid concentration of 6 M, a solution temperature of 100 ℃, and acid-treatment times of 2, 4, and 6 h are denoted as MNTs-2h, MNTs-4h, and MNTs-6h, respectively. MNTs obtained with acid concentrations of 1 and 2 M and a solution temperature of 60 ℃ for 4 days of acid treatment are denoted as MNTs-1M and MNTs-2M, respectively. MNTs obtained with an acid concentration of 2 M, a solution temperature of 70 ℃, and 2 and 3 days of acid-treatment time are denoted as MNTs-2d and MNTs-3d, respectively.

2.3 Encapsulation of Ag nanoparticles in MNTs-1M

We dissolved 100 mg of silver acetate in deionized water, added 50 mg of HNTs or MNTs, and performed sonication for 15 min. The suspension was vacuum-pumped for 30 min, and the loading of silver acetate was achieved by pulling and breaking the vacuum three times. The precipitate was washed with deionized water, dried at 80 ℃, and then heated at 300 ℃ for 1.5 h.

2.4 Aspirin loading of HNTs and MTNs

Aspirin was employed as a model guest molecule for the loading experiments. For the aspirin loading, HNTs and MNTs-2h were used as the aspirin nanocarriers. Aspirin-loaded composites were synthesized as follows. First, 100 mg of aspirin was dissolved in 50 mL of ethanol, and 100 mg of nanocarriers was then added with constant stirring for 4 h at room temperature. The mixed solution was separated by centrifugation. The filtrate was analyzed via ultraviolet–visible absorption spectroscopy (UNICO UV-2600). The amount of the drug adsorbed on the nanocarriers was calculated according to the mass balance before and after the adsorption.

2.5 Benzotriazole loading of HNTs and MNTs-1M

We dissolved 200 mg of benzotriazole in 10 mL of an acetone solution and then added 100 mg of HNTs or MNTs. The suspension was transferred to a vacuum jar and evacuated using a vacuum pump until the solvent was completely evaporated. Then, the precipitate was washed (with 20% ethanol/isooctane) and dried under vacuum. The loading efficiency was calculated according to the mass increase.

2.6 Characterization

Transmission electron microscopy (TEM) images were obtained using a JEOL JEM-200CX instrument equipped with an energy-dispersive X-ray spectroscopy (EDS) attachment at an accelerating voltage of 200 kV. N_2 adsorption–desorption isotherms were measured at −196 ℃ using a Micromeritics ASAP 2020 Sorptometer. The specific surface area was calculated using the Brunauer–Emmett–Teller (BET) method, and the total pore volume was estimated according to the amount adsorbed at a relative pressure of ~0.99. The pore-size distribution curves were calculated according to the analysis of the adsorption branch of the isotherm using the Barrett–Joyner–Halenda (BJH) algorithm. X-ray diffraction (XRD) patterns were obtained using a RigakuD/max 2550 with Cu Kα radiation (λ = 0.15406 nm) over scanning ranges of 2θ = 1°–10° for small-angle XRD (SAXRD) at a voltage of 40 kV and 300 mA and 2θ = 10°–90° for wide-angle XRD (WAXRD) at a voltage of 40 kV and 200 mA, both with a step width of 0.02°. The Fourier transform infrared (FTIR) spectra of the samples were obtained using a Nexus-670 spectrometer with a nominal resolution of 2 cm^{-1}. The effective range was 400 to 4,000 cm^{-1}. The elemental composition of the samples was determined via X-ray fluorescence (XRF, Venus 200) analysis with pressed powder. Solid-state magic-angle spinning nuclear magnetic resonance (MAS NMR) spectra were recorded using a Bruker AMX400 spectrometer to characterize the local structure around the Si and Al atoms in the samples, with frequencies of 79.49 MHz for ^{29}Si and 104.26 MHz for ^{27}Al. The aluminum concentration was determined using the titration method.

2.7 Computational details

All calculations were performed using the CASTEP code, according to first-principles DFT. Both the local-

density approximation (LDA) and the generalized gradient approximation, with the exchange-correlation potential proposed by Perdew, Burke, and Ernzerhof (PBE), were used for the calculations [43]. The ultrasoft pseudo-potential plane-wave [44] formalism and an energy cutoff of 400 eV were applied. The Monkhorst–Pack [45] grid with a sufficiently dense *k*-point mesh was used for the accurate calculation of the NMR, and the Gamma point was used for the geometrical calculations. The self-consistent total energy in the ground state was determined using the density-mixing scheme [46]. For the geometric optimization, the convergence threshold of the self-consistent field tolerance was set as 1.0×10^{-6} eV/atom, all the forces on the atoms were converged to less than 0.03 eV/Å, the total stress tensor was reduced to the order of 0.05 GPa, and the maximum ionic displacement was within 0.001 Å. The cell parameters and atomic coordination were optimized during the geometric optimization using the Broyden–Fletcher–Goldfarb–Shanno minimization algorithm. Typically, we used a 2 × 1 × 1 supercell (4 HNT units) for the calculations, unless otherwise specified. The surface structures were formed by adding 18 Å vacuum in the (001) direction, while the other cluster structures were confined in a 20A box. For Si NMR calculations, the theoretical isotropic chemical shifts, δ_{iso}, were evaluated according to the DFT-calculated isotropic shielding, σ_{iso}, via the equation $\delta_{iso} = a\sigma_{iso} + \sigma_{ref}$, by using a-quartz as a reference (δ_{isoref} = −107 pm). Because the PBE results had a linear relationship with the LDA results, the parameter a was found to be similar between the LDA and PBE results (both had a = 0.5). On the other hand, σ_{ref} was 104 and 117 ppm in the LDA and PBE results, respectively.

3 Results and discussion

As illustrated in Fig. 1, the synthesis of MNTs with a special morphology from the natural 1:1 clay mineral halloysite was achieved via acid-leaching pretreatment and a subsequent hydrothermal process. In addition to the simple acid-leaching treatment where halloysite lumen was enlarged from natural HNTs [20], nanotubes with a tunable mesoporous silica inner shell and a preserved clay outer shell were synthesized by the hydrothermal method after acid pretreatment, using CTAB as the soft template. Compared with the typical

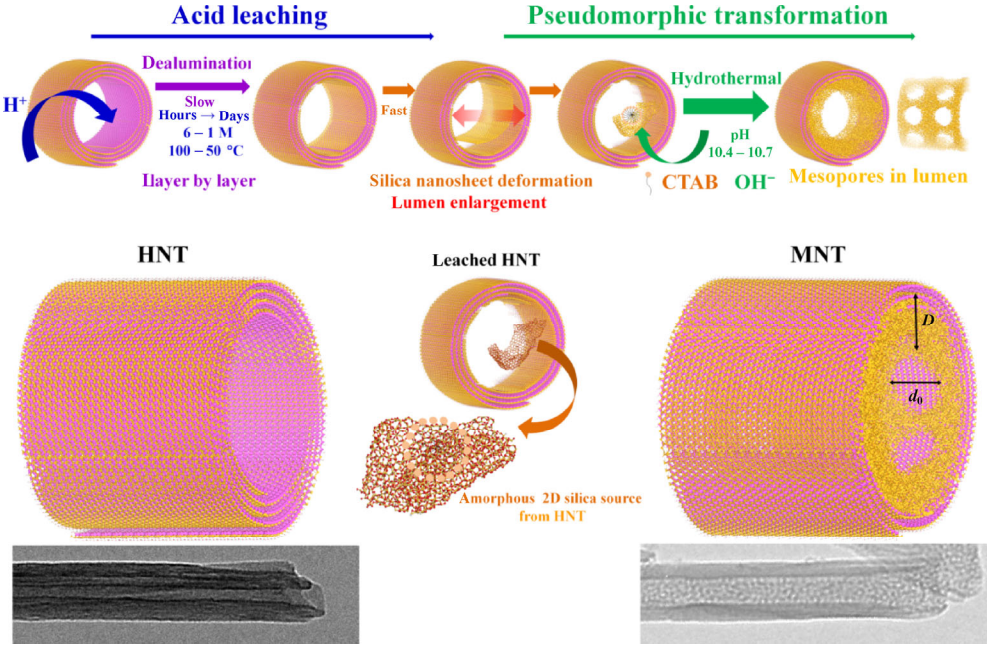

Figure 1 Illustration of the synthesis strategy from HNT to MNT. The lumen enlargement of HNT after the dealumination process of acid leaching, the formation of the amorphous 2D silica source from the deformation of the 2D silica nanosheet, and the formation of the mesoporous nanotube structure are illustrated. The inner-shell thickness (D) of the nanotube wall and the mesopore size (d_0) were tuned by changing the acid-leaching and pseudomorphic-transformation conditions.

pseudomorphic-transformation method, relatively low pH values of ~10.5 were used because of the more reformable two-dimensional (2D) silica source provided by the leached HNTs, and the clay outer shell of the nanotube remained intact. Together with experimental characterizations, DFT calculations were performed to explore the atomic structure evolution during the acid leaching and pseudomorphic transformation.

3.1 Acid-leaching process

The lumen diameter of HNTs can be conveniently controlled by regulating the acid-leaching time while exploiting different chemical properties of the inner and outer surfaces of the HNTs [20]. Considering the slight aggregation of an HNT nanoparticle gel in a sulfuric acid solution during the leaching process (Fig. S1 in the Electronic Supplementary Material (ESM)), an HCl solution was used as an alternative in this study.

Halloysite ($Al_2Si_2O_5(OH)_4 \cdot nH_2O$, n = 0–4), i.e., a layered aluminosilicate of the kaolinite group that is hydrated (halloysite-10Å) or unhydrated (halloysite-7Å) depending on n, has a tubular morphology with typical external and inner diameters of 50–100 and 10–20 nm, respectively. Accordingly, most HNT tubes have approximately 25–50 layers, although some can have less than 20 or more than 60 layers. A typical HNT tube with an external diameter of 70 nm and a lumen diameter of 13 nm has 38 aluminosilicate layers. Accordingly, there are 27, 21, and 13 layers left for 30%, 45%, and 65% leached HNTs (Fig. 2(a)). With this basic understanding, the variation of the Al leaching content throughout the acid-leaching process can be easily numerically interpreted, and the decrease in reaction slope is attributed to the diversity of the number of layers for each nanotube.

The kinetics of the halloysite-dealumination process under various acid temperatures (50–100 ˚C) and concentrations (1–6 M) were examined (Fig. 2(b)). A similar reaction order was observed at low temperatures (50–70 ˚C) using HCl, and almost the same result was obtained for 1 M sulfuric acid at 50 ˚C (open squares) by Lvov et al. (dotted line) [20]. However, the linear relationship between the Al leaching content and the leaching time deteriorated as the reaction proceeded, and the reaction slope decreased gradually. For example, at an acid concentration of 1 M, the real leaching efficiency decreased after the leached Al content exceeded 45% on average (solid line). Although the leaching rate was low at 1 M and 50 ˚C, it was

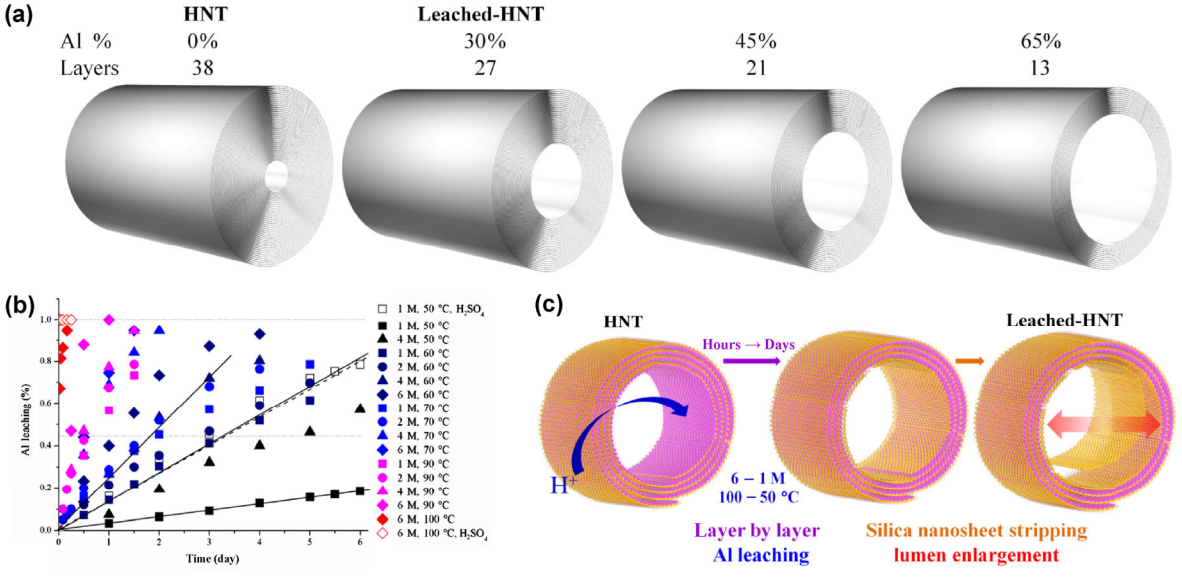

Figure 2 The decrease of the number of layers and Al content in HNT after acid leaching. (a) Tubular structure of pristine HNT and leached HNT with different layers. The corresponding leached Al content and numbers of residual HNT layers are indicated. (b) Al leaching content of halloysites with respect to time in an aqueous suspension at different temperatures and acid concentrations. The aluminum concentration was normalized with respect to the maximum, and the estimated error of the concentration determination was ±4%. The leaching content for 1 M acid at 50, 60, and 70 ˚C is fitted with a solid line. (c) Schematic of the acid-leaching process.

significantly increased at higher acid concentrations and temperatures, accelerating the reaction time from days to hours. In the acid-leaching process, the Al content in each aluminosilicate layer decreased from the inner shell to the outer shell layer-by-layer, followed by the formation of a 2D silica nanosheet and the enlargement of the lumen structure inside the halloysite tube (Fig. 2(c)).

To clarify the structural evolution of the HNTs in the acid-leaching process, a series of samples obtained under acid conditions of 6 M and 100 ℃ for x h of leaching (samples labeled as HNTs-xh) were examined to avoid the interference of the residual silica that can arise at low leaching temperatures. At the first stage of the leaching process, because of the high concentration of protons in the acid solution, Al ions were kinetically leached from the lattice structure under heating. The dealumination of the innermost aluminosilicate layer in the HNT lumen led to the formation of a 2D silica nanosheet, and the diffusion of H ions into the halloysite inner layers caused the hydroxylation of the silica surface in the lumen. After 2 h of acid leaching, the relative intensity of the reflections in the leached HNTs-2h decreased, indicating the partial loss of the crystallinity of the nanotubes (Fig. S2(a) in the ESM). The reflections disappeared as the leaching time increased, indicating the amorphization of the leached samples [20, 35]. According to the FTIR spectra of the HNTs and leached HNTs (Fig. S2(b) in the ESM), the amount of AlOH species decreased with a longer leaching time, as indicated by the disappearance of the peaks at 3,695, 3,620 (AlO–H stretching vibrations), and 910 cm^{-1} (AlO–H deformation vibration). Similar trends were observed for the peaks at 754 cm^{-1} (Al–O–Si perpendicular stretching) and 533 cm^{-1} (Al–O–Si deformation vibrations). The formation of SiOH species after the Al leaching is indicated by the broad peak corresponding to the stretching SiO–H vibrations at 3,000–3,800 cm^{-1} with a maxima at 3,400 cm^{-1}. Some asymmetric Si–O stretching vibrations around 1.020 cm^{-1} were shifted to higher wavenumbers of 1,080–1,240 cm^{-1} for the leached HNTs. The removal of Al–OH layers from the HNTs during the acid-leaching process was confirmed by XRF analysis (Table S1 in the ESM).

As the leaching proceeded, the leaching of several Al–O layers in the inner shell of the HNTs led to the formation of 2D silica nanosheets. Because of the higher strain energy at the inner shell of the HNT tubes, these nanosheets tended to curve and aggregate as small, amorphous silica nanoparticles and were weakly attached to the lumen (Fig. 3). The diffusion ability of these silica nanoparticles inside the HNT lumen was greatly enhanced by increasing the solution temperature from 70 ℃ (Fig. 3(b)) to 100 ℃ (Fig. 3(c)). These nanoparticles, which were ~10 nm in size, aggregated gradually and became sufficiently large at a higher Al-leaching level, diffusing to the outside of the tube (Fig. 3(b), inset). Thus, in addition to the general procedure of washing and centrifugation after the leaching, the separation of the silica nanoparticles from the HNTs was highly influenced by the leaching temperature, which is particularly interesting if leached HNTs with no attached residual silica nanoparticles from the leached part are desired (Fig. 3(c)). Interestingly, as the leaching proceeded, the tubular framework of the silica layers stopped curving, and the tubular morphology was maintained even for the fully leached HNTs. It appears that the stability of the tubular silica layers was high enough to resist the attenuation of the strain energy at a large tube radius (Fig. 3(d)) [47]. However, the interface structure of the innermost layers, which is crucial for functional applications such as adsorption and chemical loading, remains unclear.

3.2 Atomic structure evolution and energetics during acid leaching

It is reported that the unhydrated halloysite structure is a tubular type of kaolinite structure curving in (010) directions, and the NMR spectra for Al and Si in both structures are similar according to the literature [20, 48, 49]. The halloysite layer structure comprises a tetrahedral Si sheet and an octahedra Al sheet, which are connected by vertex oxygen centers. Three kinds of OH groups exist in the halloysite structure: the outer-surface OH in the lumen tunnel, the interlayer OH in the bulk lattice structure, and the inner OH buried within the layer between the Al sheet and the Si sheet. To study the structural evolution of the HNTs under acid leaching, a kaolinite structure was used for DFT calculations. As the dispersion energy

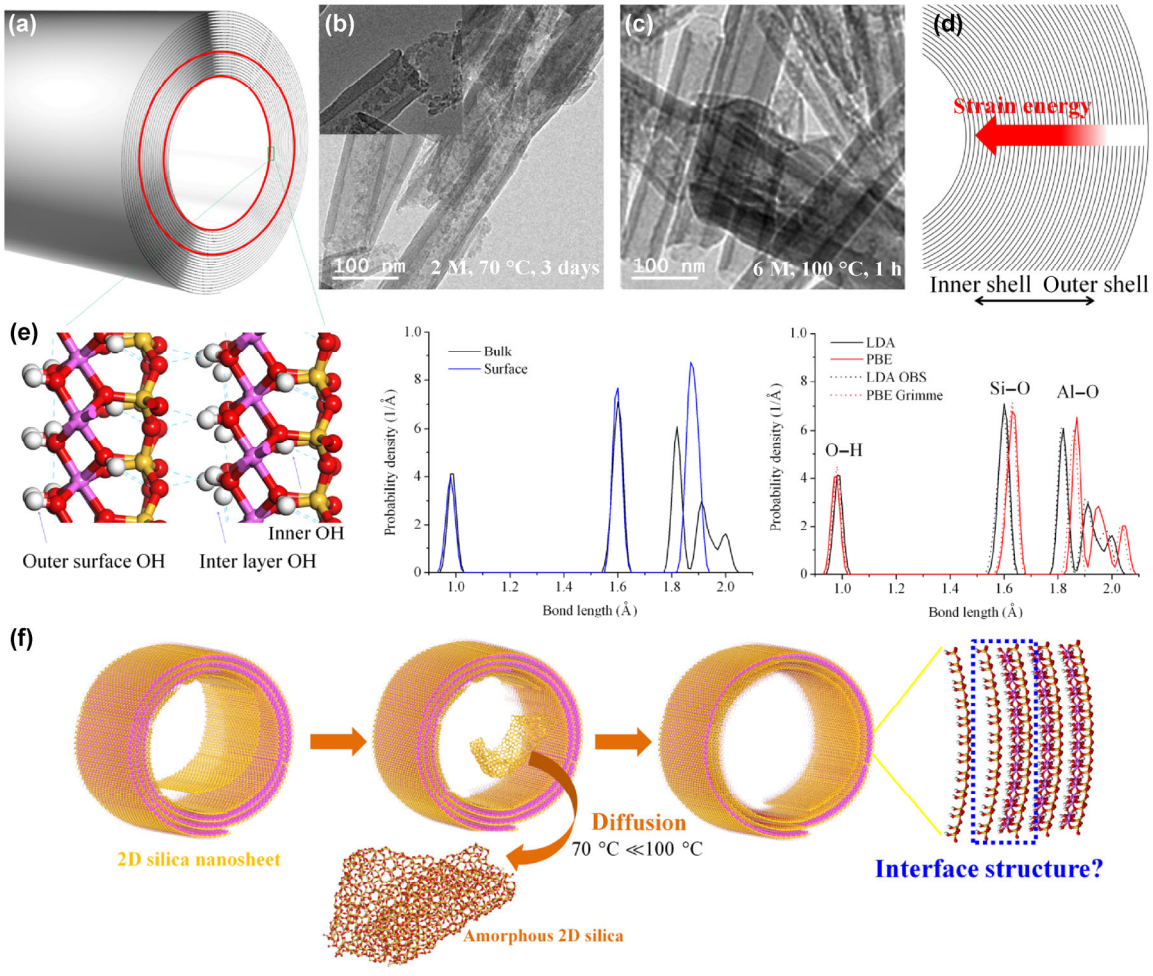

Figure 3 The lumen and interface structure of leached HNTs after acid leaching. Nanotube (a) and TEM images of halloysite with ~60% Al leached under HCl treatment of 2 M and 70 ˚C (b) or 6 M and 100 ˚C (c) for 3 days or 1 h. (d) The strain-energy distribution (arrow) in the normal direction is indicated in red. (e) Outermost surface and inner-layer structure of the HNTs and the corresponding bond distributions with LDA, PBE, LDA-OBS, and PBE Grimme functionals. (f) Structural evolution of the silica nanosheet in the halloysite lumen, as highlighted above.

may play a major role in the structure stabilization of the clay mineral because of the interaction between the layers, the PBE functional always overestimates the bond lengths, while the LDA underestimates them, as previously reported for kaolinite and montmorillonite [50, 51]. To date, several hybrid functionals, such as PBE-D2 [50], B3LYP [52], B3LYP-D [53], and RPBE-D2 [50, 53], have been adopted to reproduce the experimental layer distance [54, 55]. However, little attention has been paid to the local bonding structure. Hence, the bulk structure of the kaolinite (represented as HNTs in this case) was reexamined with a series of functionals, along with the optimized bond distances between the central cations (Si and Al) and oxygen atoms: O_a (apical O), O_b (basal O), and OH_{inn} (inner OH). A convergence test for the formation energy of pure HNTs indicated a negligible difference for E_{cutoff} higher than 400 eV for all functionals and a supercell size larger than $2\sqrt{2}\times\sqrt{2}\times1$ (Fig. S3 in the ESM).

As shown in Table 1, the relative error for LDA and PBE was nearly the same (~1%) for the lattice vectors ***a*** and ***b***. Under OBS (LDA-O) and Grimme (PBE-D2) dispersion corrections, the layer distance (vector ***c***) of the HNTs was slightly decreased by 0.06 and 0.15 Å, respectively. Although good agreement (~1% overcorrected for vector ***c***) with the experimental lattice vectors was observed for PBE-D2, the description

Table 1 Calculated and experimental unit-cell parameters and bond lengths of the HNTs. The underestimated and overestimated results are highlighted in red and blue, respectively

	LDA [50]	LDA	LDA-O	PBE [50]	PBE	PBE-D2 [50]	PBE-D2	B3LYP [52]	B3LYP-D [53]	Exp [54]	Exp [55]
a (Å)	5.11	5.08	5.04	5.214	5.207	5.177	5.18	5.17	5.16	5.15	5.15
b (Å)	8.88	8.84	8.75	9.049	9.045	8.983	8.98	8.98	9.02	8.94	8.94
c (Å)	7.17	7.14–7.6	7.08	7.459	7.473	7.313	7.3	7.43	7.4	7.39	7.4
α (°)	91.8	92.1	92.1	91.93	91.78	91.76	91.7	91.9	91.1	91.9	91.7
β (°)	105.1	104.5	104.9	104.9	104.3	105.1	104.5	105	105	105	104.6
γ (°)	89.8	89.8	89.9	89.77	89.81	89.83	89.8	89.8	89.8	89.8	89.8
Si–O_b (Å)	1.624	1.604–1.606	1.600	1.643	1.634	1.639	1.63	1.637		1.615	1.620
Si–O_a (Å)	1.597	1.577–1.591	1.573	1.619	1.61	1.615	1.605	1.610		1.615	1.610
Al–O (Å)	1.962	1.965–1.968	1.955	1.99	2.004	1.988	2.000	1.926		1.927	1.971
Al–OH_{inn} (Å)	1.921	1.906–1.887	1.905	1.939	1.937	1.942	1.941	1.858		1.913	1.921
Al–OH_{inter} (Å)	1.835	1.819–1.832	1.812	1.867	1.867	1.859	1.859	1.875		1.894	1.857

for the Si–O and Al–O bonds was unsatisfactory. Most importantly, although the Al–O_{inter} bonds well reproduced the experimental results, the change for the Al–O bonds was negligible, and the errors for the Al–OH_{inner} bonds were similar to those in PBE results. The two relaxed bulk structures obtained with the LDA and PBE functionals are shown in Fig. S4 (in the ESM). It appears that the LDA yielded better Si–O local structures, while the PBE yielded better local structures at the outer surface (Al–OH_{inter}).

Because the incorporation of 1–2 H_2O molecules in the layer space only increased the layer distance by 0.1 Å (Fig. S5 in the ESM), some water may have remained inside the unhydrated halloystie-7Å [16]. The water content in the interlayer affects the layer stacking and the energetics of the HNTs, similar to the case of layered double hydroxides [56].

Naturally, the dehydroxylation of pristine halloysite is hardly self-induced, because of the high formation energy (approximately 2–3 eV) for the dehydroxylation and dehydration processes [57]. However, while the acid solution flows into the halloysite lumen, the protons released from the acids induce the cation exchange of Al, i.e., Al leaching. The structural evolution during the dealumination of halloysite was explored using a $2\sqrt{2}\times\sqrt{2}\times1$ supercell ($Al_{16}Si_{16}O_{40}(OH)_{32}\cdot nH_2O$), in which 1 to 16 Al atoms were removed from the structure one-by-one, with the charge compensated by H (Fig. 4).

The Al leaching energy of the leached HNTs ($(Al_{16-x}Si_{16}O_{40}(OH)_{32-3x}\cdot(n+3x)H_2O$, where x is the number of leached Al) in HCl was calculated as follows: $E_l = E_{Leached\text{-}HNT} - (E_{HNT} + E_{HCl})$, where $E_{Leached\text{-}HNT}$, E_{HNT}, and E_{HCl} are the total energies of the leached HNTs, HNTs, and HCl, respectively.

At the first stage of the leaching, in the acid solution, the aluminol AlOH species on the HNT lumen surface were protonated by H^+ ions in the solution, forming positive $Al(OH_2)$ species (Fig. S6 in the ESM). These positive species weakened the bonding between Al and O, leading to the leaching of Al in the HNTs. Typically, three H^+ ions are exchanged with one lattice Al(Oh) under the charge-compensation effect. The leaching of Al breaks the Al–O–Al continuum, while the remaining Al(Oh) species might be metastable and tend to dehydroxylate and decompose into Al(V) and Al(Td) species. Along with the leaching process, the Al content in each layer decreases, and the bonding in the Al–O–Al continuum breaks. We calculated that the leaching formation energy of Al at the surface structure was ~0.2 eV lower than that in the bulk case (Fig. 4(b)).

The previously intrinsic stable Al(Oh) structures became unstable and tended to lose their hydroxyl groups during the acid-leaching process. The dehydration energy with respect to the Al leaching level (x) is shown in Fig. 4(c) (also see the local structures in Figs. S7–S9 in the ESM). While the

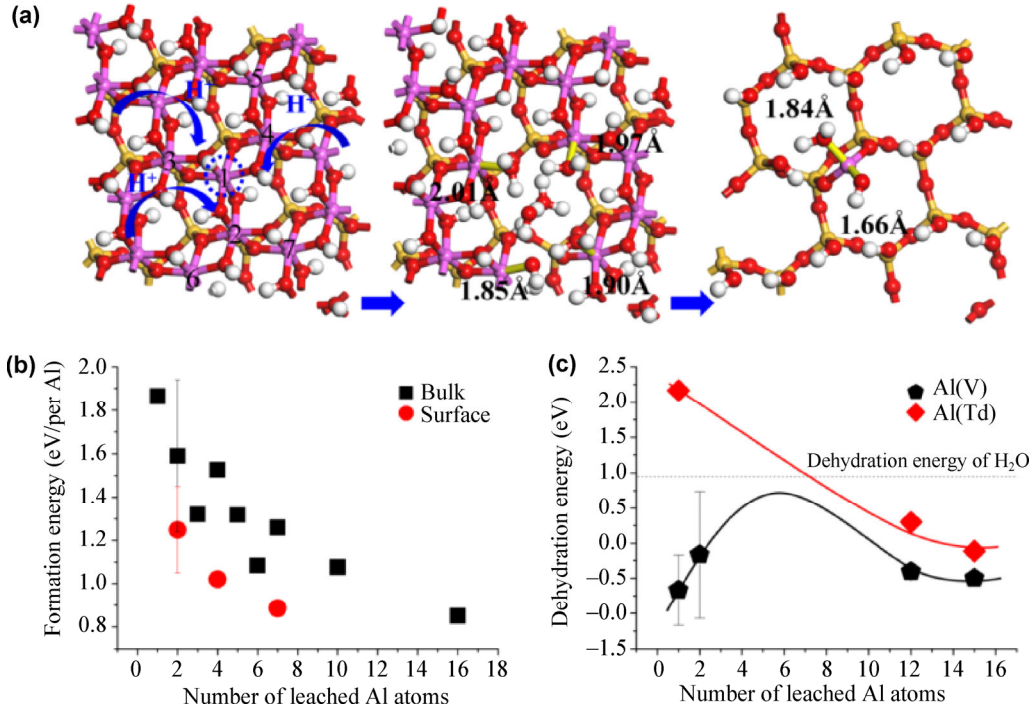

Figure 4 (a) Local structural evolution from pure HNTs ($Al_{16}Si_{16}O_{40}(OH)_{32}{\cdot}nH_2O$) to leached HNTs ($Al_{16-x}Si_{16}O_{40}(OH)_{32-3x}{\cdot}(n+3x)H_2O$) for a leaching level of x = 1 to 15. The dehydroxylation of the Al species after Al leaching. (b) Formation energy of the Al leaching for the bulk (black) and surface structure (red). (c) Dehydration energy for the transition from Al(Oh) species to Al(V) (pentagon) or Al(Td) (diamond) species at different leaching levels for the surface structure. The calculated dehydration energy of H_2O molecules in the water solution is shown as a reference (dashed line).

dehydroxylation energy from Al(Oh) to Al(V) was significantly lowered from ~2 eV before leaching to approximately −1.0–0.5 eV for the whole leaching levels (pentagon), the further dehydroxylation from Al(V) to Al(Td) decreased dramatically and occurred only at a high leaching level (diamond). At the last stage of leaching, the removal of most Al atoms in the HNTs resulted in the formation of dispersed Al species, with only two Al atoms adjacent to or even far from each other, i.e., an Al(Oh)–Al(Oh) continuum or an isolated Al(Oh) structure. These species were spontaneously dehydrated and evolved into Al(V)–Al(Oh), Al(V)–Al(V), and Al(Td)–Al(Td) species or isolated Al(Td) species. Species such as Al(Oh)–Al(V), Al(V)–Al(V), and Al(V) easily generated reactive radicals. The dehydroxylation barrier from the isolated Al(V) species to the Al(Td) species was substantially reduced at the final stage.

From an energy viewpoint, the stability of HNT decreased as the amount of leached Al increased, and the dehydration energy, i.e., the decomposition barrier of one H_2O molecule from the Al(Oh) species in the leached HNTs, was substantially reduced compared with that of pristine HNTs. This stimulated numerous reactive Al(V) species on the surface of the lumen tunnel. The dehydration barrier was increasingly in accord with the bond length of Al–OH_2 as the lower barrier increased. LDA indicated a dehydration energy ranging from −0.2 to −1.2 eV for an Al–O bond length of 1.95 to 2.22 Å. PBE indicated a similar formation energy but bond lengths 0.1 Å longer. However, the accurate description of the energy during the leaching process was complicated by the surrounding H-bonding environment. The distributions of Al–OH and Al–H_2O species on the leached-HNT surface were influenced by the lattice bending and the water content. The dehydration energy suggests modest bonding interactions of H_2O with the inner walls of the nanotubes. Compared with the vaporization enthalpy of water (44 kJ/mol), although a more accurate dehydration energy of H_2O (0.5 eV) was obtained using the PBE functional, a similar trend for the

dehydroxylation of the Al species was observed. Nevertheless, considering the poor description of the Si–O bonding by the PBE functional, as previously reported [58], for simplicity, only the LDA results are used for comparison and discussion.

3.3 Pseudomorphic transformation of HNTs into MNTs

To clarify the structural evolution of the MNTs under different conditions, MNTs-*x*h samples pretreated at an acid temperature of 100 °C were first investigated, to avoid the interference of the residual silica, as previously discussed. The low- and high-magnification TEM images shown in Fig. 5 indicate the nanotube morphology evolution, and the corresponding EDS spectra of pristine HNTs and MNTs-*x*h are shown in Fig. S10 (in the ESM). The MNTs-2h and MNTs-4h had tubular mesopores. However, for the MNTs-6h, the outermost tubular shell was partially lost and transformed into mesoporous silica. The Al content in each MNT sample decreased gradually with the leaching pretreatment, as confirmed by the EDS spectrum. After the selective etching of Al for 2 h, the MNTs exhibited a distinct tubular morphology with the mesoporous structure perforating the wall. The mesopore size was ~3 nm. Upon further acid leaching, the lumen diameters of the nanotubes increased, and the wall became increasingly thinner until it broke. Surprisingly, the tubular morphology was maintained even when the clay shell was almost lost, as for the MNTs-4h.

To produce MNT samples with better mesoporous structures, a series of MNTs-*x*M samples with noticeable pores (Fig. 6) inside the lumen were synthesized by pretreating HNTs at a lower acid concentration and heating temperature. Mesoporous silica structures at the outside of the MNTs were observed, owing to the residual silica outside the leached HNTs after the leaching process. To avoid the formation of a mesoporous structure outside the tube, the optimal Al leaching content should not exceed 60% (according to the leaching rate shown in Fig. 3).

The WAXRD pattern (Fig. 7(a)) of natural HNTs shows the characteristic reflections of HNTs (JCPDS card No. 29-1487). A diagnostic feature of the XRD pattern of halloysite with a tubular morphology is the intense (020) reflection. The broadness of the main reflections was due to the curving structure of the halloysite tubes, as confirmed by the simulated XRD pattern (pink line) of HNTs with diameter of

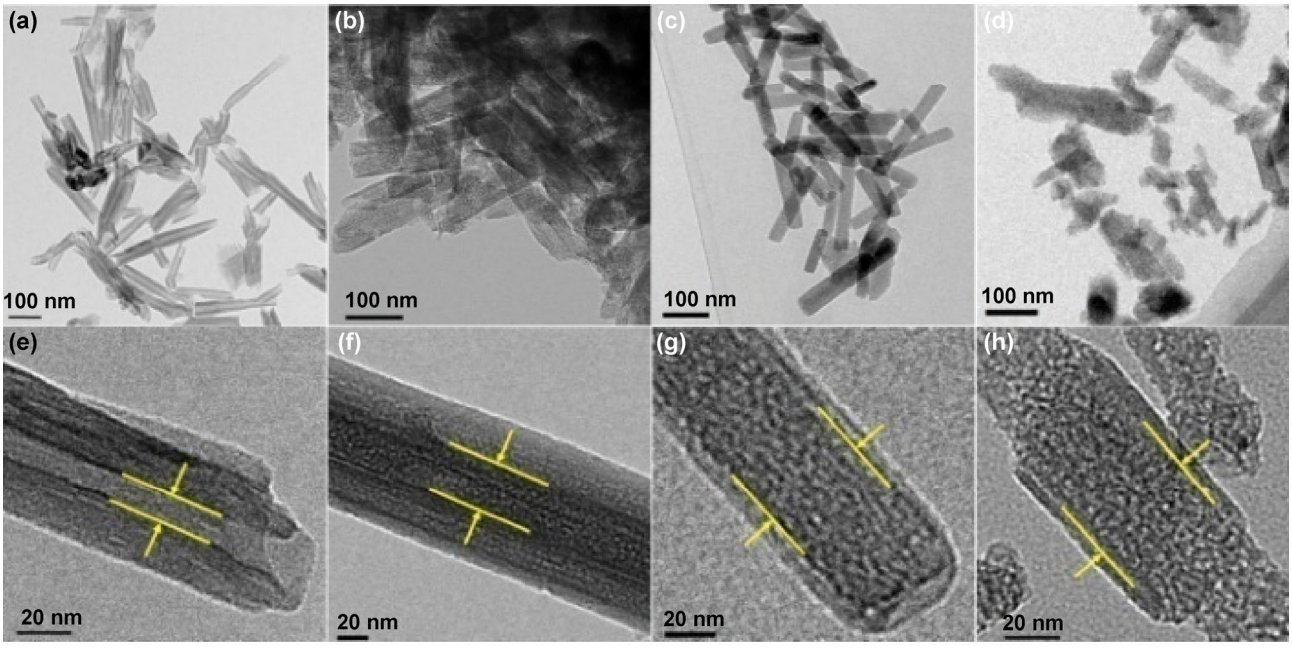

Figure 5 TEM images of pristine HNTs and MNTs. (a)–(d) Low- and (e)–(h) high-magnification TEM images of (a) and (e) pristine HNTs, (b) and (f) MNTs-2h, (c) and (g) MNTs-4h, and (d) and (h) MNTs-6h.

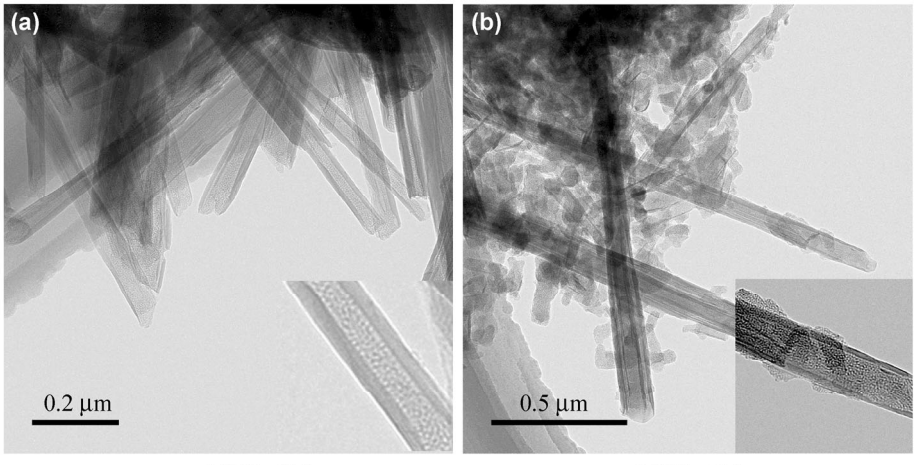

Figure 6 TEM images of MNTs with a significant mesoporous structure in the lumen. (a) MNTs-1M and (b) MNTs-2M were acid-pretreated at acid concentrations of 1 and 2 M at 60 ˚C for 4 d.

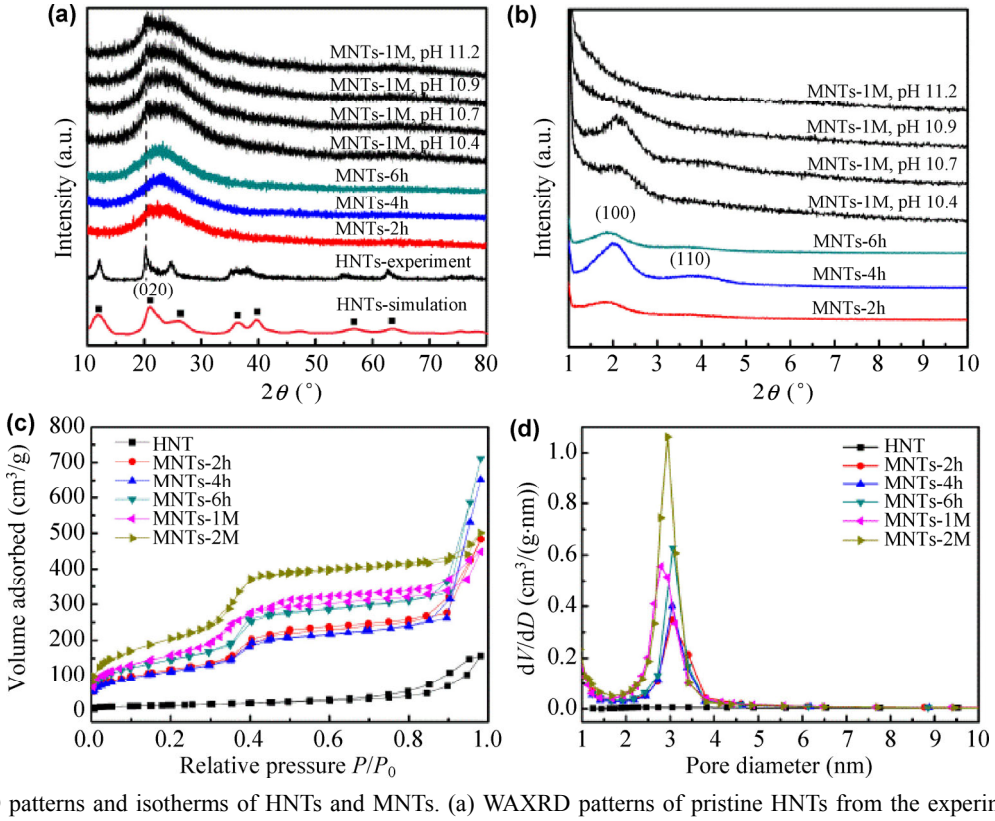

Figure 7 XRD patterns and isotherms of HNTs and MNTs. (a) WAXRD patterns of pristine HNTs from the experiment (black) and simulation (pink) and MNTs synthesized under different acid-pretreatment conditions and pH values during the hydrothermal reaction. (b) SAXRD patterns of MNTs. (c) N_2 adsorption–desorption isotherms. (d) BJH pore-size distribution.

13 nm. The mesopores in the MNTs were confirmed by SAXRD patterns (Fig. 7(b)).

Two peaks indexed to (100) and (110) diffractions were observed, which are characteristic of wormhole-like mesostructures with a uniform pore size, as shown in the TEM images (Figs. 5 and 6). The two obvious reflections indicate a higher productivity of MNTs with a relatively narrow pore-size distribution compared with previous studies [30, 59, 60]. After the hydrothermal reaction, the characteristic reflections

of the HNTs (Fig. 7(a)) and mesostructures (Fig. 7(b)) remained for the MNTs-1M samples under a pH of 10.4–10.7, while the (020) reflection of the HNTs disappeared for the MNT-*x*h samples with $x > 2$, owing to the condensation and reformation of the Si–O framework with the assistance of CTAB.

N_2 physisorption measurements were performed to analyze the textural characteristics of the HNTs (Fig. S11 in the ESM) and MNTs (Figs. 7(c) and 7(d)) at different acid-leaching times. The HNTs exhibited an H3-type hysteresis loop at a relative pressure (P/P_0) above 0.65 without any capillary condensation steps (black line) and had a BET surface area of 59 m^2/g and a total pore volume of 0.24 cm^3/g (Table S2 in the ESM). The leached HNTs exhibited a type-IV isotherm with a distinct type-H3 hysteresis loop at a P/P_0 value of 0.8–1.0, suggesting that the leached HNTs only had a small amount of irregular mesopores. This is confirmed by the BJH pore-size distribution.

In contrast, the isotherm profiles of all the MNT samples can be categorized as type-IV isotherms with an H1 hysteresis loop. The capillary condensation step in the relative pressure (P/P_0) range of 0.35–0.45 is ascribed to the typical uniform mesopores, whereas the capillary condensation step occurring in the relative pressure (P/P_0) range of 0.85–1.0 was probably due to the cavities of the macropores and tubes. The BJH pore-size distribution of the MNT samples shows sharp peaks at ~3 nm, which agrees with the TEM results. The BET specific surface areas of the MNT samples were 424, 405, and 526 m^2/g with pore volumes of 0.75, 1.01, and 1.10 mL/g, respectively (Table S2 in the ESM). These values are close to those of MCM-41 synthesized from HNTs [36]. However, significantly larger surface areas were observed for the MNTs-1M (583 m^2/g) and MNTs-2M (746 m^2/g).

3.4 Atomic structure evolution and energetics during hydrothermal process

To further investigate the local structural evolution, solid-state NMR measurements were performed (Fig. 8). To clarify the structure of the MNTs, the decomposition of the NMR spectra was performed using the Gaussian method (Fig. S12 in the ESM). In the ^{27}Al MAS NMR spectra, the three peaks at 2, 30, and 54 ppm are characteristic of the 6-, 5-, and 4-coordinated Al species, i.e., Al(Oh), Al(V), and Al(Td), respectively. The transformation from Al(Oh) species to Al(Td) species was enhanced as the leaching proceeded, whereas the Al(V) content remained at ~25%. In the ^{29}Si NMR spectra, the signal at –92 ppm corresponds to the continuum $–Si(OSi)_3OAl_2–$ structure ($–Q^3–2Al–$) in the original HNTs, and the other two signals at approximately −101 and −110 ppm are assigned to the $–Si(OSi)_3(OH)–$ (Q^3) and $–Si(OSi)_4–$ (Q^4) species, as previously reported [20, 35]. For the MNTs-2h, mostly Q^3 and Q^4 species emerged instead of $–Q^3–2Al–$ species, compared with the natural HNTs. The results indicate that H atoms replaced Al atoms during the acid-leaching process. The removal of Al and the condensation reaction of silanol groups resulted in the decrease of the wall thickness, as shown in TEM (Fig. 5). The 2D Q^3 silica units began to condense and form a Q^4 structure, whose NMR signal overlapped with the signal of the Q^4 structure of quartz at approximately −107 ppm. However, several side peaks were observed around the three main peaks (Fig. 8(b)), indicating unclarified species. For further designing such Al-leached and Si-condensed MNT materials with a complicated structure, the detailed mechanism must be clarified.

NMR spectroscopy, especially ^{29}Si NMR, is useful for examining the structural changes in minerals whose intermediate phases have poor crystallinity. For the calculated ^{29}Si NMR results, the corresponding correlation plots are shown in Fig. 8(c). Linear regressions yield the following relationship: δ_{iso} (ppm) = 0.5 × σ_{iso} + 104. Compared with the experimental NMR results, the structure for the NMR signals around –90 ppm can be assigned to various types of Si species, such as continuum $–Q^3–2Al–$, $–Q^3–Al–$, Q^3, Q^2, and Q^4 layer structures (solid line) or distorted $–Q^3–2Al–$ and $–Q^3–Al–$ structures (dot line), as indicated by the calculated NMR results (for details regarding the NMR analysis, see Figs. S13–S17 in the ESM).

The chemical shifts become less negative as the mean Si–O bond length increases, the mean Si–O–Si bond angle decreases, or the electronegativity of the surrounding groups decreases [40]. The overall trend accords with the general rules, i.e., a smaller amount of Al bonded to the Q^3 structure yields a more negative NMR shift. However, the real reason for this

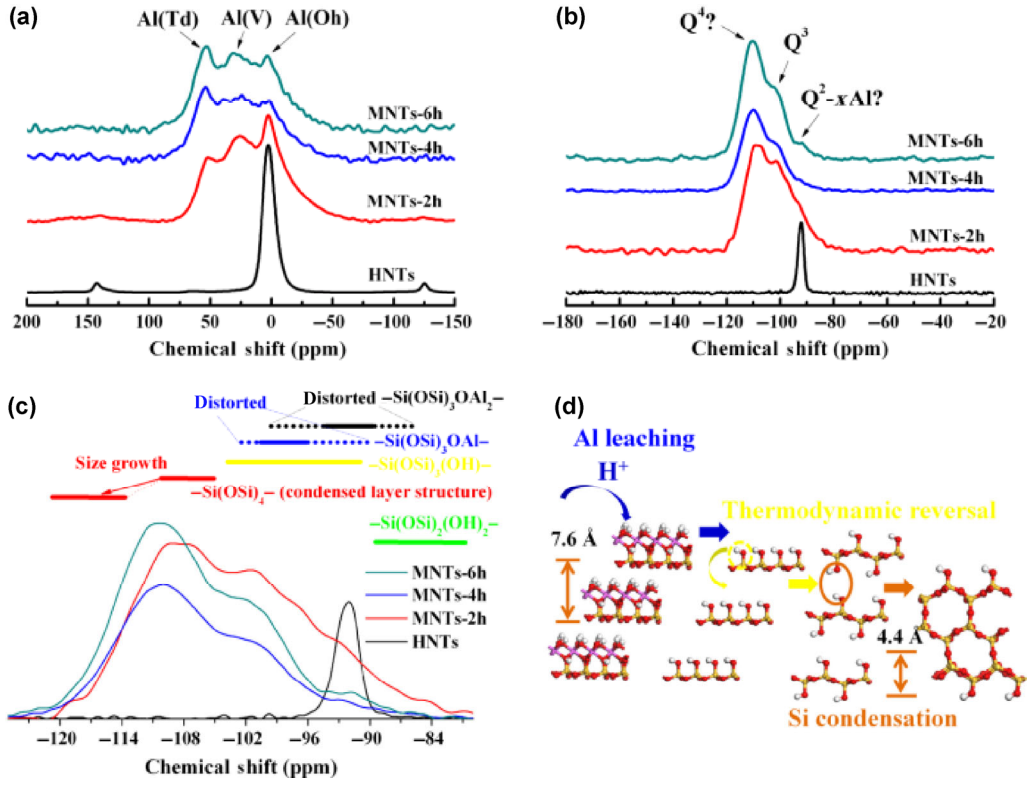

Figure 8 NMR spectra of HNTs and MNTs. (a) ^{27}Al MAS NMR and (b) ^{29}Si MAS NMR spectra of pristine HNTs (black line) and MNTs with different inner diameters under different leaching times of 2 h (red line), 4 h (blue line), and 6 h (cyan line). (c) ^{29}Si MAS NMR spectra analysis based on DFT calculations. The chemical-shift range for the –Q^3–2Al– (black), –Q^3–Al– (blue), Q^3 (yellow), and Q^2 (green) structures are given. The ranges for the corresponding distorted structures are indicated by the dotted lines. (d) Possible silica condensation scheme under hydrothermal reactions after Al leaching.

phenomenon is the distortion of the local structure around Si due to the H-bonding reorientation under the Al leaching.

The Si-condensation mechanism of MNTs with a tunable thickness is proposed in Fig. 8(d). While the silica condensation caused by the interaction between the acid-induced Si–OH and the inert outer Si–O surface is energetically unfavorable, the proton attack caused by the optimal acid/base concentrations or the controlled hydrothermal conditions can result in a transition from an inert Si–O surface to an active Si–OH surface [61] or the thermodynamic reversal of Si–OH groups from the inner surface to the outer surface. The inert outer surface of Si–O in HNT samples from mineral sources is occasionally hydroxylated owing to the proton attack in the natural geological environment (Fig. S18 in the ESM). After the leaching process, the thermal flip of the Si–OH groups induced under the hydrothermal condition facilitates the silica-condensation process. Hence, when the stability of dealuminated structures are substantially decreased after acid leaching, the condensation begins, and Al-containing MNTs with tunable inner diameters can thus be engineered with the interlayer distance changed from 7.6 to 4.8–4.4 Å, depending on the detailed condensation topology. The interlayer distance between the Si layers is not significantly changed during the Al leaching process (repulsion from the H bond between Si–OH) until the Si condensation occurs, and the dehydroxylation between Si–OH groups occurs only after the distances between the Si–OH layers are in the valence-bonding range.

According to the previous discussion, for the pseudomorphic transformation from leached HNTs to MNTs, the local structural evolution and hydroxylation energy of the silica framework during the hydrothermal reactions are proposed (Fig. 9).

According to the hydroxylation energies of the 2D

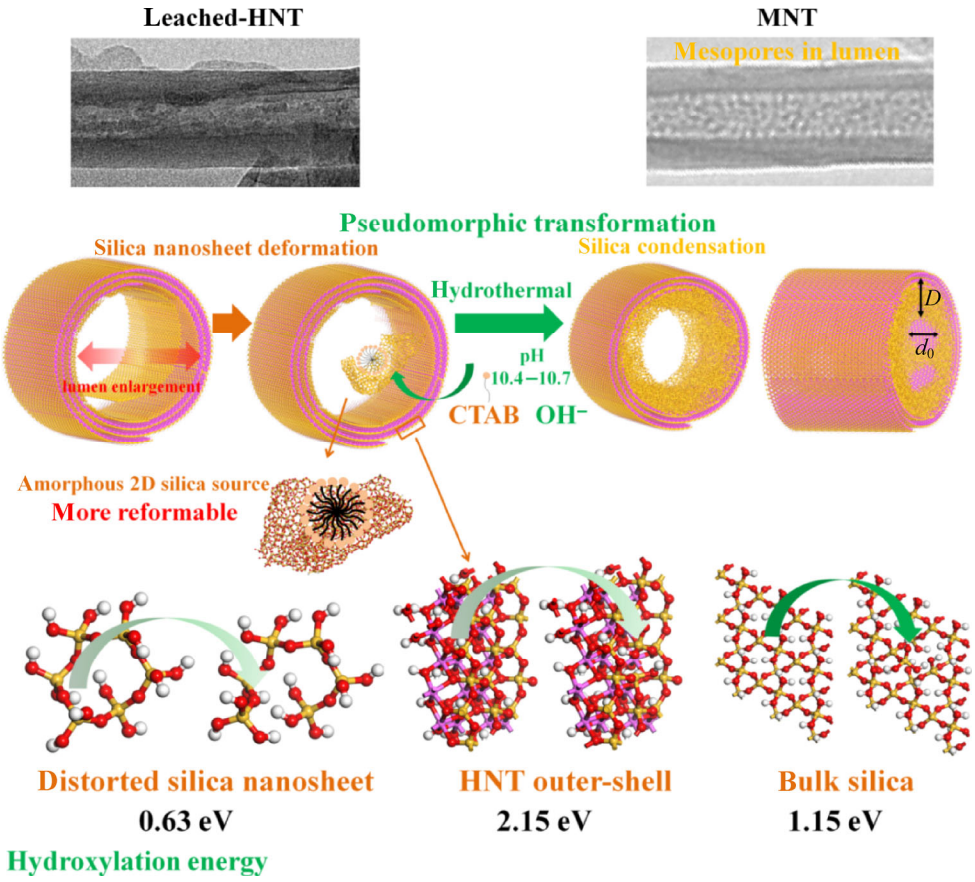

Figure 9 The pseudomorphic transformation from leached HNTs to MNTs. The local structural evolution of the silica framework during the hydrothermal reactions. The hydroxylation energies of the 2D silica nanosheet, the HNT outer shell, and the bulk silica quartz are indicated.

silica nanosheet, the HNT outer shell, and bulk silica quartz, the major reason for the structural transformation under a lower alkaline pH is the lower hydroxylation energy of the 2D silica nanosheet compared with that of the bulk silica quartz. The HNT outer shell remained intact because of the high stability of the natural clay shell. The inner diameter of the MNTs increased with the amount of Si layers that were condensed, and the mesoporous structures were introduced in the halloysite framework by the CTAB template during the hydrothermal reaction. The diffusion of the acid-etched $Si(OH)_4$ species around the mesopore edges may have resulted in the intercalation of Si to the interlayer (Fig. S19 in the ESM), and the Si leaching led to the transformation from the layered Si–O structure to the disordered silica structure. Considering the large distance between the hydrated silica layers for the MNTs-2h sample, the Q^4 structure was probably formed under this diffusion mechanism at the first stage.

Hence, for the MNTs mesoporous structures, the origin of the various local structures formed around Si can be divided into three parts (Figs. 10(a) and 10(b)): (1) the reactive –Q^3–2Al(V)– and –Q^3–Al(V)– species formed after Al leaching by the proton attack of the acid, (2) the Q^2 species at the mesopore edges formed after Si leaching under the hydrothermal reaction with the CTAB template, and (3) the Q^4 species formed by the silica reformation during the acid leaching and the condensation during the pseudomorphic-transformation process.

3.5 Enhanced loading ability of MNTs

To demonstrate that the MNT material is a promising carrier for loading biological and chemical substances, MNTs were used as nanocontainers for Ag loading

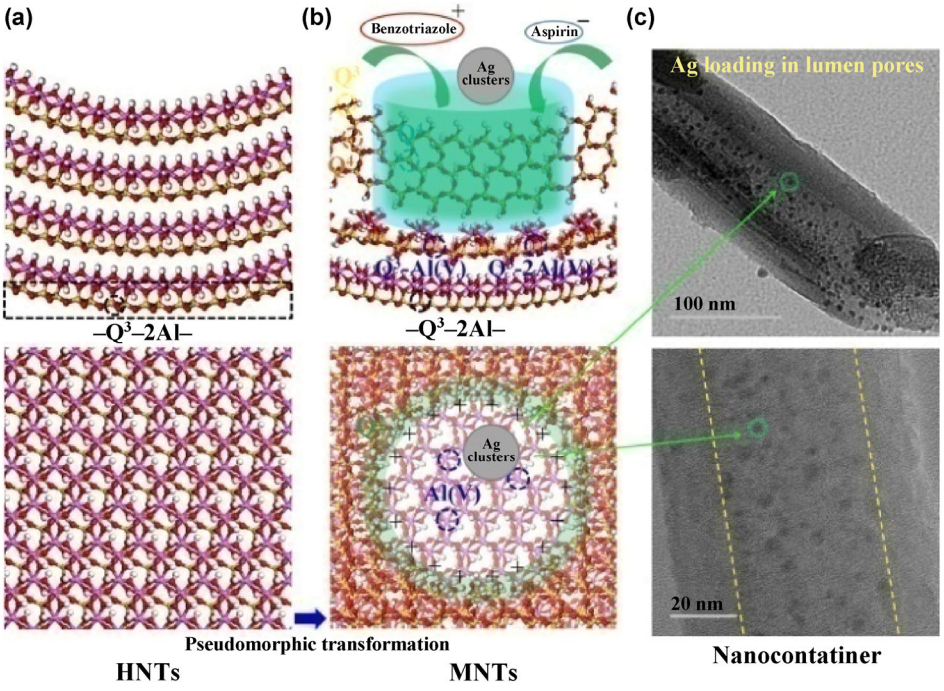

Figure 10 The interface structure for HNTs and MNTs. Side and top views of the atomic structure for (a) HNTs and (b) MNTs. The predominant Si/Al species of $–Q^3–2Al–$, $–Q^3–2Al(V)–$, $–Q^3–Al(V)–$, Q^4, Q^3, and Q^2 are shown. (c) TEM images of the MNTs used as nanocontainers for Ag loading in the lumen pores of MNTs, where one Ag nanoparticle confined in a mesopore is highlighted.

(Fig. 10(c)), Ag nanoparticles were well-confined within the mesopores in the lumen structure (yellow line) of MNTs with an average particle size of ~4 nm. The loading of anticorrosion (benzotriazole) and drug (aspirin) chemicals in the MNTs was also performed. The benzotriazole loading efficiency for the MNTs-2d (50%) was higher than that of simply acid-treated HNTs (30%) or pristine HNTs (16%). The aspirin loading for the MNTs-2h (157 mg/g) was 5 times larger than that of the HNTs (33 mg/g) and larger than the amounts of aspirin loaded in MCM-41 [62] (100 mg/g) and zeolites HY [63] (106 mg/g). The high drug-loading capacity is mainly attributed to the large surface area (inherited from the mesoporous structures in the nanotube lumen) and the high adsorption ability of the residual Al–OH groups in the outer shell. Compared with other silica-nanotube materials [7, 8] and mesoporous-silica materials [9, 38, 59], the MNTs, having numerous mesopores inside the nanotube lumen and the preserved clay shell, had a larger surface area than the silica nanotubes and a larger half-closed lumen space to serve as a nanocontainer. Different drug-release behaviors within such mesostructures are expected. Thus, the as-synthesized MNTs have potential as eco-friendly nanocarriers for chemical loading.

4 Conclusions

A novel approach for synthesizing MNTs from HNTs by introducing mesopores inside the nanotube lumen structure via an improved pseudomorphic transformation method is proposed. A well-defined mesoporous nanotube container with a varying inner mesoporous silica thickness and a preserved outermost clay shell was obtained by exploiting the chemical components and morphology of natural clay. Using DFT calculations, the atomic structure evolution and the energetics during the processes of Al leaching and Si–OH condensation were investigated in detail, and various Al and Si species were identified via NMR analysis. The silica from the leached HNTs, i.e., amorphous silica nanosheets, was more reformable (pH = 10.5) than other silica sources. Introducing mesoporous structures in the inner walls of the acid-leached halloysite clay (typically 50% dealumination at a low leaching

temperature and acid concentration) yielded excellent eco-friendly nanocontainers for Ag loading. The MNTs-2d exhibited a high chemical loading owing to the introduction of mesopores in the tube lumen and the preservation of the adsorptive species in the halloysite outer shell. Our successful preparation of MNTs may provide new insights into the controllable synthesis of novel nanomaterials with a special morphology from natural clay minerals.

Acknowledgements

This work was supported by the National Natural Science Foundation of China (Nos. 41572036 and 51225403), the Hunan Provincial Science and Technology Project (Nos. 2016RS2004 and 2015TP1006) and the National "Ten Thousand Talents Program" in China. Computing resources were provided by High Performance Computing Centre of Central South University and the National Supercomputing Center of China in Shenzhen. We acknowledge Yalin Xia, Huilin Lun and Binbin Guo for their kind help in sample preparation, characterization and drug loading experiment.

Electronic Supplementary Material: Supplementary material (TEM, SEM, XRF, XRD, FTIR and BET results for acid-leached HNTs and MNTs samples, dehydroxylation of Al(V) species, progressive intercalation of Si, and NMR results from DFT calculations) is available in the online version of this article at https://doi.org/10.1007/s12274-017-1482-x.

References

[1] Zhang, K.; Xu, L. L.; Jiang, J. G.; Calin, N.; Lam, K. F.; Zhang, S. J.; Wu, H. H.; Wu, G. D.; Albela, B.; Bonneviot, L. et al. Facile large-scale synthesis of monodisperse mesoporous silica nanospheres with tunable pore structure. *J. Am. Chem. Soc.* **2013**, *135*, 2427–2430.

[2] Yang, J. P.; Shen, D. K.; Wei, Y.; Li, W.; Zhang, F.; Kong, B.; Zhang, S. H.; Teng, W.; Fan, J. W.; Zhang, W. X. et al. Monodisperse core–shell structured magnetic mesoporous aluminosilicate nanospheres with large dendritic mesochannels. *Nano Res.* **2015**, *8*, 2503–2514.

[3] Lee, I.; Zhang, Q.; Ge, J. P.; Yin, Y. D.; Zaera, F. Encapsulation of supported Pt nanoparticles with mesoporous silica for increased catalyst stability. *Nano Res.* **2011**, *4*, 115–123.

[4] Mao, C. B.; Wang, F. K.; Cao, B. R. Controlling nanostructures of mesoporous silica fibers by supramolecular assembly of genetically modifiable bacteriophages. *Angew. Chem., Int. Ed.* **2012**, *51*, 6411–6415.

[5] Obare, S. O.; Jana, N. R.; Murphy, C. J. Preparation of polystyrene- and silica-coated gold nanorods and their use as templates for the synthesis of hollow nanotubes. *Nano Lett.* **2001**, *1*, 601–603.

[6] Ma, Z.; Dai, S. Development of novel supported gold catalysts: A materials perspective. *Nano Res.* **2011**, *4*, 3–32.

[7] Kang, D. Y.; Brunelli, N. A.; Yucelen, G. I.; Venkatasubramanian, A.; Zang, J.; Leisen, J.; Hesketh, P. J.; Jones, C. W.; Nair, S. Direct synthesis of single-walled aminoaluminosilicate nanotubes with enhanced molecular adsorption selectivity. *Nat. Commun.* **2014**, *5*, 3342.

[8] Martin, C. R.; Kohli, P. The emerging field of nanotube biotechnology. *Nat. Rev. Drug Discov.* **2003**, *2*, 29–37.

[9] Vallet-Regí, M.; Balas, F.; Arcos, D. Mesoporous materials for drug delivery. *Angew. Chem., Int. Ed.* **2007**, *46*, 7548–7558.

[10] Yu, J.; Yang, C.; Li, J.; Ding, Y. C.; Zhang, L.; Yousaf, M. Z.; Lin, J.; Pang, R.; Wei, L. B.; Xu, L. L. et al. Multifunctional Fe_5C_2 nanoparticles: A targeted theranostic platform for magnetic resonance imaging and photoacoustic tomography-guided photothermal therapy. *Adv. Mater.* **2014**, *26*, 4114–4120.

[11] Molina, E.; Warnant, J.; Mathonnat, M.; Bathfield, M.; In, M.; Laurencin, D.; Jéroîme, C.; Lacroix-Desmazes, P.; Marcotte, N.; Gérardin, C. Drug-polymer electrostatic complexes as new structuring agents for the formation of drug-loaded ordered mesoporous silica. *Langmuir* **2015**, *31*, 12839–12844.

[12] Zhou, X. J.; Moran-Mirabal, J. M.; Craighead, H. G.; McEuen, P. L. Supported lipid bilayer/carbon nanotube hybrids. *Nat. Nanotechnol.* **2007**, *2*, 185–190.

[13] Charlier, J. C.; Blase, X.; Roche, S. Electronic and transport properties of nanotubes. *Rev. Mod. Phys.* **2007**, *79*, 677–732.

[14] Han, W. Q.; Yu, H. G.; Zhi, C. Y.; Wang, J. B.; Liu, Z. X.; Sekiguchi, T.; Bando, Y. Isotope effect on band gap and radiative transitions properties of boron nitride nanotubes. *Nano Lett.* **2008**, *8*, 491–494.

[15] Deng, S. Z.; Fan, H. M.; Wang, M.; Zheng, M. R.; Yi, J. B.; Wu, R. Q.; Tan, H. R.; Sow, C. H.; Ding, J.; Feng, Y. P. et al. Thiol-capped ZnO nanowire/nanotube arrays with tunable magnetic properties at room temperature. *ACS Nano* **2010**, *4*, 495–505.

[16] Joussein, E.; Petit, S.; Churchman, J.; Theng, B.; Righi, D.; Delvaux, B. Halloysite clay minerals—A review. *Clay Miner.* **2005**, *40*, 383–426.

[17] Lvov, Y.; Wang, W. C.; Zhang, L. Q.; Fakhrullin, R. Halloysite clay nanotubes for loading and sustained release of functional compounds. *Adv. Mater.* **2016**, *28*, 1227–1250.

[18] Wang, J. H.; Zhang, X.; Zhang, B.; Zhao, Y. F.; Zhai, R.; Liu, J. D.; Chen, R. F. Rapid adsorption of Cr(VI) on modified halloysite nanotubes. *Desalination* **2010**, *259*, 22–28.

[19] Luo, P.; Zhang, J. S.; Zhang, B.; Wang, J. H.; Zhao, Y. F.; Liu, J. D. Preparation and characterization of silane coupling agent modified halloysite for Cr(VI) removal. *Ind. Eng. Chem. Res.* **2011**, *50*, 10246–10252.

[20] Abdullayev, E.; Joshi, A.; Wei, W. B.; Zhao, Y. F.; Lvov, Y. Enlargement of halloysite clay nanotube lumen by selective etching of aluminum oxide. *ACS Nano* **2012**, *6*, 7216–7226.

[21] Yuan, P.; Southon, P. D.; Liu, Z. W.; Kepert, C. J. Organosilane functionalization of halloysite nanotubes for enhanced loading and controlled release. *Nanotechnology* **2012**, *23*, 375705.

[22] Lvov, Y. M.; Shchukin, D. G.; Möhwald, H.; Price, R. R. Halloysite clay nanotubes for controlled release of protective agents. *ACS Nano* **2008**, *2*, 814–820.

[23] Abdullayev, E.; Price, R.; Shchukin, D.; Lvov, Y. Halloysite tubes as nanocontainers for anticorrosion coating with benzotriazole. *ACS Appl. Mater. Interfaces* **2009**, *1*, 1437–1443.

[24] Shchukin, D. G.; Sukhorukov, G. B.; Price, R. R.; Lvov, Y. M. Halloysite nanotubes as biomimetic nanoreactors. *Small* **2005**, *1*, 510–513.

[25] Du, M. L.; Guo, B. C.; Jia, D. M. Newly emerging applications of halloysite nanotubes: A review. *Polym. Int.* **2010**, *59*, 574–582.

[26] Yah, W. O.; Takahara, A.; Lvov, Y. M. Selective modification of halloysite lumen with octadecylphosphonic acid: New inorganic tubular micelle. *J. Am. Chem. Soc.* **2012**, *134*, 1853–1859.

[27] Zhai, R.; Zhang, B.; Liu, L.; Xie, Y. D.; Zhang, H. Q.; Liu, J. D. Immobilization of enzyme biocatalyst on natural halloysite nanotubes. *Catal. Commun.* **2010**, *12*, 259–263.

[28] Zhang, Y.; He, X.; Ouyang, J.; Yang, H. M. Palladium nanoparticles deposited on silanized halloysite nanotubes: Synthesis, characterization and enhanced catalytic property. *Sci. Rep.* **2013**, *3*, 2948.

[29] Yu, Y. T.; Qiu, H. B.; Wu, X. W.; Li, H. C.; Li, Y. S.; Sakamoto, Y.; Inoue, Y.; Sakamoto, K.; Terasaki, O.; Che, S. Synthesis and characterization of silica nanotubes with radially oriented mesopores. *Adv. Funct. Mater.* **2008**, *18*, 541–550.

[30] Zhang, A. F.; Hou, K. K.; Gu, L.; Dai, C. Y.; Liu, M.; Song, C. S.; Guo, X. W. Synthesis of silica nanotubes with orientation controlled mesopores in porous membranes via interfacial growth. *Chem. Mater.* **2012**, *24*, 1005–1010.

[31] White, R. D.; Bavykin, D. V; Walsh, F. C. The stability of halloysite nanotubes in acidic and alkaline aqueous suspensions. *Nanotechnology* **2012**, *23*, 065705.

[32] Zhang, A. B.; Pan, L.; Zhang, H. Y.; Liu, S. T.; Ye, Y.; Xia, M. S.; Chen, X. G. Effects of acid treatment on the physico-chemical and pore characteristics of halloysite. *Colloid. Surf. A: Physicochem. Eng. Asp.* **2012**, *396*, 182–188.

[33] Joo, Y.; Sim, J. H.; Jeon, Y.; Lee, S. U.; Sohn, D. Opening and blocking the inner-pores of halloysite. *Chem. Commun.* **2013**, *49*, 4519–4521.

[34] Ouyang, J.; Guo, B. B.; Fu, L. J.; Yang, H. M.; Hu, Y. H.; Tang, A. D.; Long, H. M.; Jin, Y. L.; Chen, J.; Jiang, J. L. Radical guided selective loading of silver nanoparticles at interior lumen and out surface of halloysite nanotubes. *Mater. Des.* **2016**, *110*, 169–178.

[35] Zhang, Y.; Fu, L. J.; Yang, H. M. Insights into the physicochemical aspects from natural halloysite to silica nanotubes. *Colloid. Surf. A: Physicochem. Eng. Asp.* **2012**, *414*, 115–119.

[36] Xie, Y. L.; Zhang, Y.; Ouyang, J.; Yang, H. M. Mesoporous material Al-MCM-41 from natural halloysite. *Phys. Chem. Miner.* **2014**, *41*, 497–503.

[37] Yang, H. M.; Tang, A. D.; Ouyang, J.; Li, M.; Mann, S. From natural attapulgite to mesoporous materials: Methodology, characterization and structural evolution. *J. Phys. Chem. B* **2010**, *114*, 2390–2398.

[38] Wu, S. H.; Mou, C. Y.; Lin, H. P. Synthesis of mesoporous silica nanoparticles. *Chem. Soc. Rev.* **2013**, *42*, 3862–3875.

[39] Galarneau, A.; Iapichella, J.; Bonhomme, K.; Di Renzo, F.; Kooyman, P.; Terasaki, O.; Fajula, F. Controlling the morphology of mesostructured silicas by pseudomorphic transformation: A route towards applications. *Adv. Funct. Mater.* **2006**, *16*, 1657–1667.

[40] MacKenzie, K. J. D.; Smith, M. E. *Multinuclear Solid-State NMR of Inorganic Materials*; Pergamon: London, 2002.

[41] Navrotsky, A. Thermochemistry of nanomaterials. *Rev. Mineral. Geochem.* **2001**, *44*, 73–103.

[42] Sahu, S. K.; Unruh, D. K.; Forbes, T. Z.; Navrotsky, A. Energetics of formation and hydration of a porous metal organic nanotube. *Chem. Mater.* **2014**, *26*, 5105–5112.

[43] Perdew, J. P.; Burke, K.; Ernzerhof, M. Generalized gradient approximation made simple. *Phys. Rev. Lett.* **1996**, *77*, 3865–3868.

[44] Vanderbilt, D. Soft self-consistent pseudopotentials in a generalized eigenvalue formalism. *Phys. Rev. B* **1990**, *41*, 7892–7895.

[45] Monkhorst, H. J.; Pack, J. D. Special points for Brillouin-zone integrations. *Phys. Rev. B* **1976**, *13*, 5188–5192.

[46] Kresse, G.; Furthmüller, J. Efficient iterative schemes for *ab initio* total-energy calculations using a plane-wave basis set. *Phys. Rev. B* **1996**, *54*, 11169–11186.

[47] Guimarães, L.; Enyashin, A. N.; Seifert, G.; Duarte, H. A. Structural, electronic, and mechanical properties of single-walled halloysite nanotube models. *J. Phys. Chem. C* **2010**, *114*, 11358–11363.

[48] Ashbrook, S. E.; McManus, J.; MacKenzie, K. J. D.; Wimperis, S. Multiple-quantum and cross-polarized ^{27}Al MAS NMR of mechanically treated mixtures of kaolinite and gibbsite. *J. Phys. Chem. B* **2000**, *104*, 6408–6416.

[49] Du, C. F.; Yang, H. M. Investigation of the physicochemical aspects from natural kaolin to Al-MCM-41 mesoporous materials. *J. Colloid Interface Sci.* **2012**, *369*, 216–222.

[50] Tunega, D.; Bučko, T.; Zaoui, A. Assessment of ten DFT methods in predicting structures of sheet silicates: Importance of dispersion corrections. *J. Chem. Phys.* **2012**, *137*, 114105.

[51] Peng, K.; Fu, L. J.; Ouyang, J.; Yang, H. M. Emerging parallel dual 2D composites: Natural clay mineral hybridizing MoS_2 and interfacial structure. *Adv. Funct. Mater.* **2016**, *26*, 2666–2675.

[52] Tosoni, S.; Doll, K.; Ugliengo, P. Hydrogen bond in layered materials: Structural and vibrational properties of kaolinite by a periodic B3LYP approach. *Chem. Mater.* **2006**, *18*, 2135–2143.

[53] Ugliengo, P.; Zicovich-Wilson, C. M.; Tosoni, S.; Civalleri, B. Role of dispersive interactions in layered materials: A periodic B3LYP and B3LYP-D* study of $Mg(OH)_2$, $Ca(OH)_2$ and kaolinite. *J. Mater. Chem.* **2009**, *19*, 2564–2572.

[54] Bish, D. L. Rietveld refinement of the kaolinite structure at 1.5 K. *Clays Clay Miner.* **1993**, *41*, 738–744.

[55] Neder, R. B.; Burghammer, M.; Grasl, T. H.; Schulz, H.; Bram, A.; Fiedler, S. Refinement of the kaolinite structure from single-crystal synchrotron data. *Clays Clay Miner.* **1999**, *47*, 487–494.

[56] Shivaramaiah, R.; Navrotsky, A. Energetics of order–disorder in layered magnesium aluminum double hydroxides with interlayer carbonate. *Inorg. Chem.* **2015**, *54*, 3253–3259.

[57] Nisar, J.; Århammar, C.; Jämstorp, E.; Ahuja, R. Optical gap and native point defects in kaolinite studied by the GGA-PBE, HSE functional, and GW approaches. *Phys. Rev. B* **2011**, *84*, 075120.

[58] Yang, H. M.; Li, M.; Fu, L. J.; Tang, A. D.; Mann, S. Controlled assembly of Sb_2S_3 nanoparticles on silica/polymer nanotubes: Insights into the nature of hybrid interfaces. *Sci. Rep.* **2013**, *3*, 1336.

[59] Bian, S. W.; Ma, Z.; Zhang, L. S.; Niu, F.; Song, W. G. Silica nanotubes with mesoporous walls and various internal morphologies using hard/soft dual templates. *Chem. Commun.* **2009**, 1261–1263.

[60] Zhang, Y. H.; Liu, X. Y.; Huang, J. G. Hierarchical mesoporous silica nanotubes derived from natural cellulose substance. *ACS Appl. Mater. Interfaces* **2011**, *3*, 3272–3275.

[61] Temuujin, J.; Okada, K.; MacKenzie, K. J. D.; Jadambaa, T. The effect of water vapour atmospheres on the thermal transformation of kaolinite investigated by XRD, FTIR and solid state MAS NMR. *J. Eur. Ceram. Soc.* **1999**, *19*, 105–112.

[62] Datt, A.; El-Maazawi, I.; Larsen, S. C. Aspirin loading and release from MCM-41 functionalized with aminopropyl groups via co-condensation or postsynthesis modification methods. *J. Phys. Chem. C* **2012**, *116*, 18358–18366.

[63] Datt, A.; Fields, D.; Larsen, S. C. An experimental and computational study of the loading and release of aspirin from zeolite HY. *J. Phys. Chem. C* **2012**, *116*, 21382–21390.